RESEARCH ARTICLE

Robust Design of Induction Machines for High-Speed Electric Freight Locomotive Applications

FARSHID MAHMOUDITABAR AND **NICK J. BAKER**, (Member, IEEE)

School of Engineering, Newcastle University, NE1 7RU Newcastle upon Tyne, U.K.

Corresponding author: Farshid Mahmouditabar (farshid.mahmouditabar@newcastle.ac.uk)

ABSTRACT This paper showcases a systematic procedure to design the most efficient re design of a commercially available induction machine to be used as a traction motor in an Electric Freight Locomotive for the rail journey from Tehran to Mashhad. Using Taguchi optimization, copper and aluminium wound versions of the machine are optimized for an 1870-ton load locomotive with a peak power of 1203kW. The driving cycle is summarized using the K-means clustering method to obtain representative points. Full details of the drive cycle and guiding rail adhesion modelling are given and subsequently used in a sequential multi-physics and multi-operation mode robust procedure which optimizes the geometry and cooling parameters whilst taking manufacturing tolerances into account. The paper thus presents a thorough comparative study of aluminium-based and copper-based designs to meet a realistic Electric Freight Locomotive specification. Results indicated that the proposed approach is effective in optimum and robust design of conventional and aluminium induction machines and can be applied to other machine types operating on other rail journeys. Switching to aluminium is one way of improving the recyclability of motors, but in the scenario considered here, results in a 1.1% reduction in efficiency over the driving cycle.

INDEX TERMS Electric freight locomotive, induction motor, taguchi, manufacturing tolerances, K-means, robust design.

I. INTRODUCTION

One of the most economic ways to transport cargo and loads for long distances is via Electric Freight Locomotives (EFL). The benefits of electrified rail travel include less pollution, a wider range of control, and quick start-stop. The traction requirements are for high cruising speed, low acceleration time, and high gradeability. The Induction Machine (IM) is often preferred in EFLs because it is mechanically robust and can present high overload capabilities, low cost, and the possibility to be employed in a multiple drive, where two or four motors are connected in parallel to one converter [1].

The optimum design of traction motors should consider the performance and cooling system over a representative driving cycle. Ideally, this should be combined with manufacturing tolerances via a systematic design procedure.

All fabrication and assembly processes are known to have tolerances and uncertainties which influence the torque performance, such as residual Permanent Magnet (PM) flux density, PM dimensions, a non-uniform airgap and lamination material degradation due to punching and wire-cutting [2], [3]. In wire cut laminations, the wire thickness affects the tolerance, where a 2 mm thick wire may result in a tolerance of 0.04 mm, significantly impacting the airgap.

Material diversities can result in the degradation in electric motor performance. For example, the tolerances for the remanent flux density of the PMs, the thickness and length of the PMs, and the thickness of the electrical steels are listed in the manufacturer's datasheet as 5%, 1%, and 8 to 10%, respectively [4]. Therefore, it is necessary to consider these uncontrolled tolerances in a proper and robust design [5].

The associate editor coordinating the review of this manuscript and approving it for publication was Pinjia Zhang.

Using aluminum instead of copper for electric motors has many advantages such as low cost, better recyclability, lower environmental costs, and less mass (direct effect on increasing torque density) [6]. However, using aluminum for the stator windings is challenging. Lower electrical conductivity may reduce volume efficiency and increase the size of the windings and thus the mass of the motor. The decision between copper and aluminum-based IMs is therefore an interesting design choice.

Regarding the optimum shape design of stator slot and rotor bar of the IM, Ref. [7], presents the design principles of an IM used in a hybrid electric vehicle (EV), considering the effects of starting, operating performance, and harmonics. In [8], a parametric study was conducted to examine the effect of stator and rotor slot dimensions on various performance parameters, and an evolutionary algorithm was used for IM design optimization. In [9], to improve the performance of 11kW IM, an optimization method based on the rotor slot type, stator slot type, steel sheet and rotor material has been conducted. In [10], by modifying the stator slot dimension and winding configuration, the efficiency class and power factor of the 1.1 kW IM have been improved from IE2 to IE3. In [11], instead of the Finite Element Method (FEM) model, the sub-domain analytical model for an axial flux IM has been used and optimization has been done over the driving cycle. In [12], using the sub-domain model, a sequential process is introduced for optimal design of IMs with and without consideration of overload in a multi-physics environment and whilst considering the driving cycle. In [13], a meta-model-based approach has been proposed to optimize the machine using a two-stage process. The machine is initially electromagnetically optimized to find the best balance of active weight and efficiency over the drive cycle. The obtained design is then thermally optimized to meet the continuous performance requirements. In [14] a series of empirical and mathematical relationships is systematically applied to reduce the number of possible Stator Slot Rotor Bar (SSRB) combinations of IM as a traction motor. Then, the admissible optimal combinations are optimized over the driving cycle. In [15], a 200 kW 370 N.m IM has been designed with the target of enhancing the performance for mass production. To achieve this goal, suitable materials and manufacturing processes like rotor die-casting, hairpin stator winding, and a specific cooling system have been investigated. In [16], to accurately size the thermo-electromagnetic parts of a low cost totally enclosed fan IM, the FEM model and thermal model are coupled.

A. ROBUST DESIGN
In mass production, robust optimization should be utilized to reduce the impact of unpredictable factors and find an optimal design with the least sensitivity to tolerance of the design parameters. The goal in conventional optimization is to obtain the global optimal point using mathematical computation and FEM analysis. The global optimum point performs perfectly, but the routine takes no consideration

of the manufacturing tolerances and material diversities. However, when considering manufacturing tolerances, the performance characteristics can be significantly lowered in the case of a slight deviation in the design parameters and could therefore increase the rate of obsolescence in mass production [17]. Contrarily, with a robust design, although the theoretical optimum performance could be below the global optimum, the motor design is robust against parasitic parameter variation and the rate of manufacturing obsolescence will hence be significantly reduced.

B. TAGUCHI OPTIMIZATION
Generally, there are three approaches to robust design: Taguchi, worst case scenario, and design for Six-Sigma. The merits and drawbacks of these methods are comprehensively investigated in [18] and [19]. The Taguchi method is widely used and preferable due to the limited number of FEM runs required. However, this method can only use a limited number of parameter levels and is unable to solve multi-objective optimizations. To overcome the first issue space reduction methods are employed and for the second one, weighted sum and fuzzy interface systems are utilized to convert multi-objective problems to single-objective problems. The robust optimization procedure requires high computational time and memory when considering the uncertainties. Therefore, in some papers, surrogate models like kriging model [3] and response surface methodology [20] are used to replace the FEM model and reduce the computational time. To further reduce the computational time sequential and multi-level methods are introduced in [21] and [22]. In these papers, the design parameters are divided into two groups of less-important and more-important parameters using Sensitivity Analysis (SA). Then, the more important design parameters are considered in the robust design process. For example, in [23], a multi-level robust optimization procedure is implemented. Firstly, using surrogate model an optimum design point is calculated. Then, by considering the manufacturing tolerance of each variable, a robust solution is determined.

C. CONTRIBUTION
In the literature, the authors have found no published work on the systematic and robust design of IM for high speed EFL applications. Therefore, the contribution of this work is to present a systematic procedure for the conceptual design of a traction motor for EFL by extracting the specification of the required powertrain and proposing a sequential multi-physics and multi-operation mode robust optimization procedure to simultaneously optimize the geometry and cooling system parameters. The results are used to inform a comparative analysis of copper and compressed aluminum-based IMs for an EFL drive cycle.

II. LOCOMOTIVE MODELLING
The general specifications of a traction motor can be calculated from the defined characteristics of the EFL, and vehicle considered. An examination of the EFL's dynamic behavior

A. RESISTIVE EFFORT

is crucial in this context. The dynamic modeling approach involves representing the vehicle body as a lumped mass situated at the center of gravity [24]. The focus is exclusively on dynamics in one direction, specifically the longitudinal forward direction, with the assumption that vehicle stability is consistently maintained. The dynamic characteristics of the EFL can be defined through the interplay between tractive and resistive forces acting on the wheels, leading to either negative or positive acceleration. Derivation of both these forces is provided in the subsequent sections.

A. RESISTIVE EFFORT

Locomotive resistive forces consist of rolling, gravity resistance and curve components as Eq. 1.

$$R_{resistive} = R_{rolling} + R_{gravity} + R_{curve} \qquad (1)$$

1) ROLLING RESISTANCE FORCE

The Davis formula is used to calculate the rolling resistance [25]. The general formulation of Davis formula is as Eq. 2. It consists of three terms as follows.

$$R_{Davis} = f(w) + bV + \frac{CAV^2}{wn} \qquad (2)$$

1. Constant with respect to speed but variable with respect to weight per axle (journal friction, rolling resistance, and track resistance),

2. Resistance proportional to the speed and consisting of wheel flange, concussion, swaying, oscillation frictions.

3. Resistances proportional to the square of the speed and consisting of air pressure effect.

Where, w_L and w_W are the axle weight of the locomotive and wagon, respectively, A is the front cross-sectional area of the train, and V is the speed of the train (km/h). In this formula, different relationships are presented for locomotives and wagons according to their design and technical characteristics. For freight locomotives, Eq. 3 and 4 are used. These formulas are obtained using the experimental tests on the resistance of standard types of freight cars of various weights and loadings under mild and severe weather conditions. The detailed formulation procedure for deriving these equations, applicable to both freight locomotives and other locomotive types, has been extensively discussed in reference [25].

$$R_{Loco} \left(N/ton \right) = 5.785 + \frac{129}{w_L} + 0.2136 \times V$$
$$+ \frac{0.00023 \times A \times V^2}{w_L \times n_L} \qquad (3)$$

$$R_{Car} \left(N/ton \right) = 5.785 + \frac{129}{w_W} + 0.3204 \times V$$
$$+ \frac{0.000049 \times A \times V^2}{w_W \times n_W} \qquad (4)$$

where, R_{Loco} is the specific resistance of the locomotive on a line, R_{Car} is the specific resistance of the wagon, n_L and n_W are the number of axles per locomotive and wagon, respectively.

2) GRAVITY RESISTANCE FORCE

The gravity resistance effort is shown in the form of a specific resistance in terms of weight and is independent of the speed of the train. This effort is equal to $F_G(\frac{N}{ton}) = mg\sin(\alpha)$.

3) CURVE RESISTANCE FORCE

The curve resistance effort, which applies when the train is traveling around a curve, is also defined in terms of curve degree and is equal to $F_{curve} \left(\frac{N}{ton} \right) = 3.55D$.

In locomotive applications, Minimum Continuous Speed (MCS) is defined as the lowest speed at which a locomotive can operate continuously under heavy load conditions without damaging the traction motors. The considered EFL is designed to be able to continuously move 22 freight cars with an average slope of 1.5 %, a weight of each wagon of 85 tons and an (MCS) of 70 km/h. The load line of the locomotive for the load of 1870 tones and slope of 1.5% is calculated according to Eq. 1.

B. TRACTIVE EFFORT

The tractive effort of the locomotive is obtained from the overlap of the traction effort produced by the traction motors and the adhesion effort of the locomotive.

1) ADHESION EFFORT

The adhesion effort represents the maximum effort that can be applied to a locomotive without the wheel slipping. Slipping of the wheels leads to severe damage to the rail. Therefore, it is necessary to correctly determine the adhesion effort and control the applied traction effort. The adhesion effort of the locomotive can be calculated as Eq. 5.

$$F_T = \sum_{i=1}^{n} \mu_i \times w_i \times g \qquad (5)$$

where, F_T is the total adhesion effort of the locomotive, μ_i is the coefficient of adhesion of wheel i, w_i is the adhesion weight applied to wheel i, n is the total number of driving axels, and g is the gravitational acceleration.

To derive the adhesion limitation curve of a locomotive it is necessary to know the weight and the variation of the adhesion coefficient versus speed. Various empirical relationships have been presented in literature based on measuring the friction coefficient between the wheel and the rail at different speeds. Four common models are Columb, Gimenez, Rational, and Exponential friction [26]. The general trend is that with increasing locomotive speed, the maximum available adhesion coefficient decreases, therefore the adhesion effort of the locomotive must also reduce. For example, Eq. 6 can be used to obtain the adhesion curve of a 138-ton (23 tons per axle) locomotive.

$$\mu = 0.3697 - 0.001489 \, V(\frac{km}{h}) \qquad (6)$$

The intersection of the load lines and adhesion limitation curve is illustrated in Fig. 1 (a). According to the obtained curve, to achieve a speed of 70 km/h, a net force of 360 kN
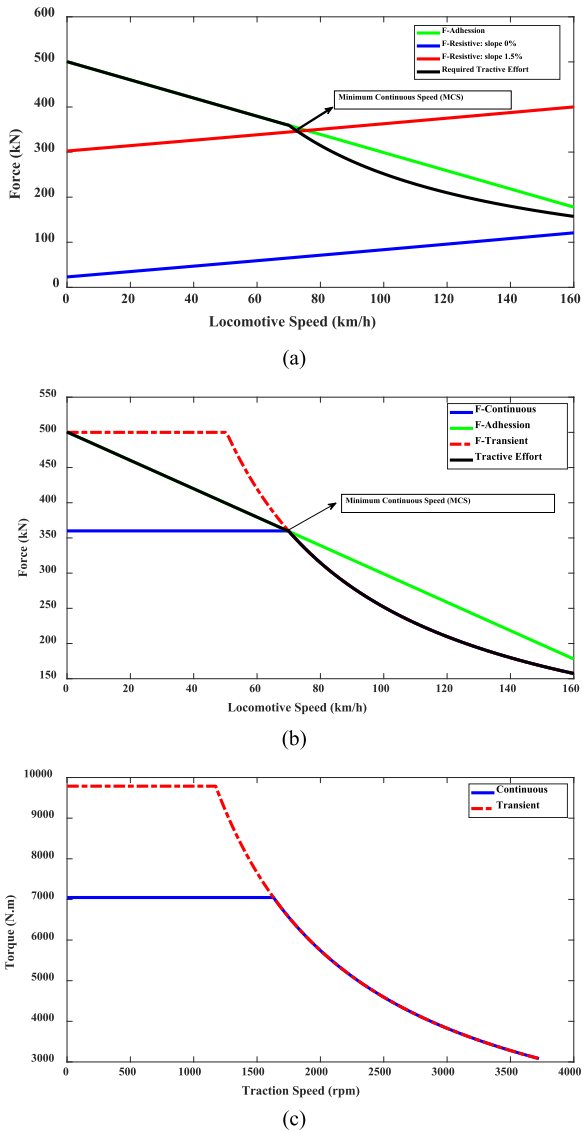
FIGURE 1. (a) The interaction of locomotive adhesion limitation and the load lines of the locomotive, (b) the required force-speed curve of the EFL at continuous and transient conditions, and (c) the required torque-speed curve of the traction motors at continuous and transient conditions.

is required, equal to a net power of 7 MW at the wheels. Therefore, the required tractive effort of the locomotive is illustrated in Fig. 1 (a). Up to 70 km/h, the required tractive effort is limited by adhesion and above 70 km/h it is limited by the net power of 7MW.

2) TRACTION EFFORT
The traction effort of locomotives is usually produced by between 4 and 6 motors, depending on the bogie structure. By increasing the dimensions of the motor, it is possible to design a traction drive with a high torque that nominally covers the entire adhesion curve of the locomotive. However, locomotive traction motors are installed on the bogie which has restricted dimensions to fit the railway standards.

TABLE 1. The details of the required traction motor.

No.	Parameter	Continuous	Transient
1	Power (kW)	1203	1203
2	Base Speed (rpm)	1630	1174
3	Base Torque (N.m)	7046	9787
4	Maximum Speed (rpm)	3725	3725
5	$V_{L\text{-}L}$ (rms)	1900 V	
6	Cooling Solution	Air Forced	
7	Insulation Class	H	

TABLE 2. The details of the existed traction motor.

Item	Description	Item	Description
Power	425 kW	Rotor outer diameter	496 mm
Supply voltage	1400 V	Air gap	2 mm
Nominal Current	240 A	Axial length	470 mm
Maximum speed	2500 rpm	Cooling	1.4 m3/s
Pole	6	The weight of rotor	790 kg
Stator outer diameter	725 mm	The weight of stator	1303 kg

The details of MCS are determined based on the load handling requirements. For example, in freight diesel-electric locomotives the value of the MCS is about 20 km/h whereas for EFL it is about 60 to 80 km/h. In this study, the MCS is 70 km/h. The traction motors must be designed to deliver nominal power for speeds higher than MCS and also be capable of overload working below the MCS for a transient period. The relationship between the required tractive force at continuous and transient conditions is shown in Fig. 1 (b). Generally, in road traction, for transient operation both torque and power are increased. In rail, however, the value of the power in both conditions remains constant while the torque value is increased.

C. TRACTION MOTOR SPECIFICATION
As implied by the continuous and transient traction force, the motors should be able to produce the equivalent force of 360 kN continuously and 500 kN for a 1-hour transient condition. The considered bogie structure in this study is Co-Co. Co-Co is the wheel arrangement for diesel and electric locomotives with two six-wheeled bogies with all axles powered, with a separate traction motor per axle. Therefore, the total number of traction motors in EFL is 6. The gearbox ratio of $n_g = \frac{18}{79}$, the wheel radius of $r_w = 0.5\ m$, and the transmission efficiency of $\eta_g = 0.97$ and equations like Eq. 7, the required torque-speed curve of traction motor is obtained. The required torque-speed curve of traction motor is illustrated in Fig. 1 (c).

$$N_b\ (\text{rpm}) = V_{L,continous}\left(\frac{km}{h}\right) \times \frac{1\left(\frac{m}{s}\right)}{3.6\left(\frac{km}{h}\right)} \times \frac{60(s)}{1(\text{minute})}$$
$$\times \frac{1(round)}{2\pi r_w(m)} \times n_g \qquad (7)$$

Finally, according to the calculated torque-speeds, the required characteristics for traction are presented in Table 1. This is now used to provide a conceptual motor design prior to implementing design optimization.
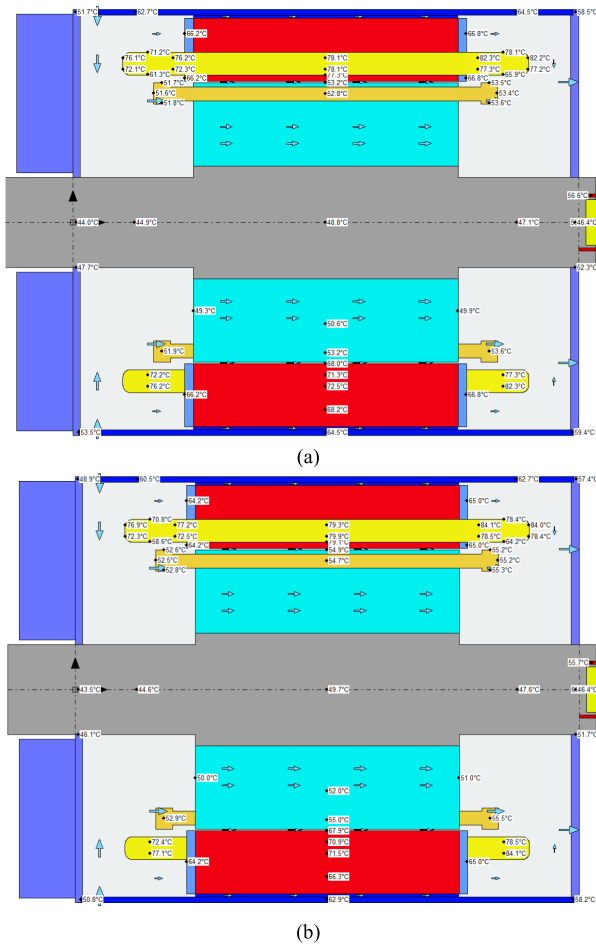
FIGURE 2. Thermal distribution at a power of 425 kW (a) 1500 rpm and (b) 2500 rpm.

FIGURE 3. The predicted power and traction torque curve of the primary motor using Motor CAD software.

Regarding the typical values of the Constant Power Speed Region (CPSR) for traction motors in EFL applications, it is essential to account for the adhesion limitations between the rail and wheel. The reported typical values for the adhesion coefficient between the rail and wheel range from 0.3 to 0.42. In contrast, EVs using tyres may experience an increase in the adhesion coefficient, reaching up to 0.85. Consequently, in EVs, it becomes feasible to enhance the applied torque on the wheel and design a machine with a broader CPSR. For example, in [27], it was noted that for a dump truck, the CPSR should be around 10:1. However, implementing a wide CPSR is not practical in Locomotive applications, where the CPSR typically ranges between 2 and 3. This limitation is due to the fact that higher CPSR values necessitate increased applied force on the wheel, consequently elevating the risk of slipping. Therefore, the design of locomotive traction motors must strike a balance between achieving an adequate CPSR and mitigating the potential for wheel slippage.

III. INITIAL DESIGN
Traction motors are installed in the bogie frame and the outer diameter and axial length are restricted by many factors.
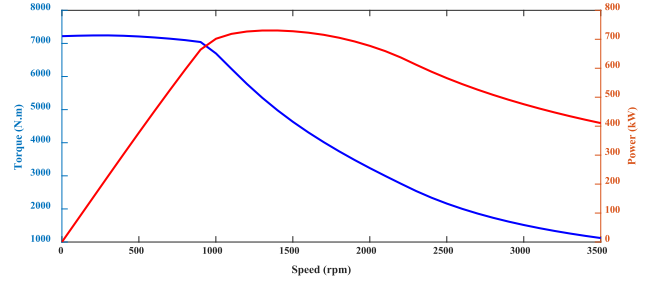
Therefore, to have a realistic design, the existing traction motor which was designed for diesel-electric locomotives is considered as a case study. The details of the considered traction motor are as Table 2.

FEM Results Validation: To verify the accuracy of the implemented electromagnetic-thermal model of the under-study traction motor, the winding resistance, no-load current, and SC current of the motor at the temperature of 20°C is measured and compared with FEM results.

The winding resistance, no-load current ($400V - 50Hz$), and locked rotor current ($230V - 50Hz$) of both FEM and experimental results were in the acceptable ranges of $42.26 < R < 46.70$ $m\Omega@20°C$, $31.5 < I_{no-load} < 33A$, and $245 < I_{Locked-rotor} < 248A$, respectively. Therefore, the implemented FEM model is validated, and this model is considered for further studies.

Implement the Multi-physics Analysis Model: Lumped Parameter Model (LPM) [28] is an equivalent circuit method for expressing the thermal characteristics of electric motors. The studied traction motor, its cooling air passage and the external air forced fan cooling characteristics are implemented in Motor CAD software. In the stator sections, four air ducts are considered for cooling. Also, two rows of axial holes are considered in the rotor. The forced air enters radially through the inlet air vent located on top of the frame in the drive-end side. It passes through the stator ducts, rotor holes, and air gap then exits through the mesh cover located on the non-drive end cover.

To obtain the nominal temperature distribution, a forced air flow rate of 1.4 m^3/s and a temperature of 40 degrees Celsius is considered. Two-way electromagnetic-thermal analysis has been carried out to extract the steady state temperature distribution of the considered traction motor. The temperature distribution at a power of 425 kW and speeds of 1500 rpm (nominal base speed) and 2500 rpm (a working point in the constant power-speed region) are shown in Fig. 2 (a) and (b), respectively. Typically, in induction machines the hot spot temperature corresponds to the end winding of the stator. In the considered IM, due to the direction of the cooling air flow, the stator's end winding in the non-drive end has the highest working temperature. The temperature of the inlet cooling air in the drive-end section (left side of Fig. 2) is the lowest and the average temperature of the element is

lower than for the non-drive-end side of the IM. For instance, for both working speeds, the hot spot temperature in the non-drive end side is almost 8°C higher than the drive-end side. However, the overall temperatures of the IM's parts at both speeds are marginally lower than the critical values and indicate that this motor can safely deliver higher output power.

The Envelope Curve of the Under-study Traction Motor: According to the calculated temperatures, the traction motor under study can deliver 425 kW and higher powers. Therefore, to check the accuracy of this issue, multi-physics analysis with defined windings and cage temperature limitations is carried out to extract the capability curve of the motor. The maximum working temperature of the coils is determined by the class of electrical insulation given in the IEC 60085 standard. In railway applications, the standard of IEC60349-2 specifies the acceptable temperature of winding classes of the traction motors. For class H insulation, the threshold limit for maximum working temperature (hotspot) is 180°C. Commonly, in the electromagnetic-thermal design of electric machines, the temperature limit for hotspot of the coils is considered one level lower, due to not considering the losses related to the drive harmonics, windage losses, and stray losses for example. Therefore, in the simulation, the maximum allowable temperature is set on insulation class F (155°C). The capability curve of the traction motor at 1400 V is shown in Fig. 3. This traction motor is designed for low-base speed applications. However, it can deliver 730 kW at a speed of 1400 rpm and a torque of 7040 N.m at a speed of 900 rpm.

The traction motor is over-designed and with some modifications to its design it is possible to enhance the performance and meet the EFL requirements. It should be noticed that in this study the outer stator and axial length of the motor remain constant to avoid re-design of the bogie.

A. DESIGN TIPS TO ENHANCE PERFORMANCE

To improve the traction motor, it is necessary to adapt the torque-speed curve to the EFL requirements. For this purpose, two traction motors will be designed.

Firstly, copper is used for the stator windings and rotor bar.

In the second design, compressed aluminum coils are proposed for the stator windings and die-casting is considered as the manufacturing process of the rotor cage. Aluminum is said to be more sustainable and have a lower environmental impact than copper [29]. The manufacturing process requirements and assumptions of both designs are discussed in the following paragraphs.

EFLs require a higher based speed, so to achieve this goal it is necessary to apply the following changes:

1) Increasing the working voltage of the motor from 1400 to 1900 Volts (the usual voltage range in EFL).
2) Use of thinner lamination lower core loss material for stator and rotor core due to increase in the working frequency and applied voltage. The material is changed from M600-65A to M400-50A.
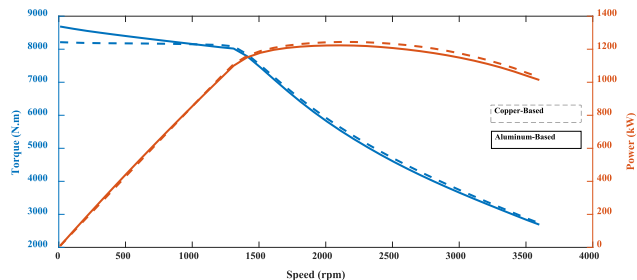

FIGURE 4. The envelope curve of the copper-based and aluminium-based design.

3) Change the stator winding type from hairpin to stranded and consequently changing the stator slot type from parallel slot to parallel tooth. The reason is that the nominal working speed of traction motor for EFL is twice that of diesel electric locomotive, therefore, the AC losses will increase, and it is not suitable to use hairpin winding anymore.
4) Changing the number of turns of the stator coils from 16 to 14 to adjust the required base speed.
5) Changing the stator winding strand numbers to meet the coil fill factor of 0.5 for copper-based design and 0.67 for compressed coil aluminum-based design.
6) Increasing the air-cooling flow from 1.4 to 4 m³/s to increase the cooling capability of the traction motor.

The SSRB combination plays an important role in the torque ripple and harmonics context of the IM. The general rules regarding selection of SSRB combination are discussed in detail in [14]. The current SSRB (54 stator slots and 44 rotor bars) meets the mentioned requirements and rules. Therefore, this combination has not changed and remains constant.

B. MANUFACTURING CONSIDERATION

The following mass production processes relating to aluminum and copper windings are incorporated into the design processes:

1) COPPER WINDINGS

Copper cage IMs can be produced in two ways: brazing or die cast. The melting temperature of copper is significantly higher than aluminum (1085°C vs 660°C). Therefore, the use of the diecast process for copper cage IM requires very resistant and high-cost molds, which will lead to a significant increase in production costs. In addition, the mold will be damaged after a period and will need to be replaced. Hence, it is more economical and conventional to use the brazing process. If the Brazing process is selected, after welding the rotor bars to the end cage, it is necessary to stabilize the position of the rotor bars in the rotor slot by using the pounding process. Therefore, the rotor slot must be an open slot type. This feature will be considered in the robust design optimization section.
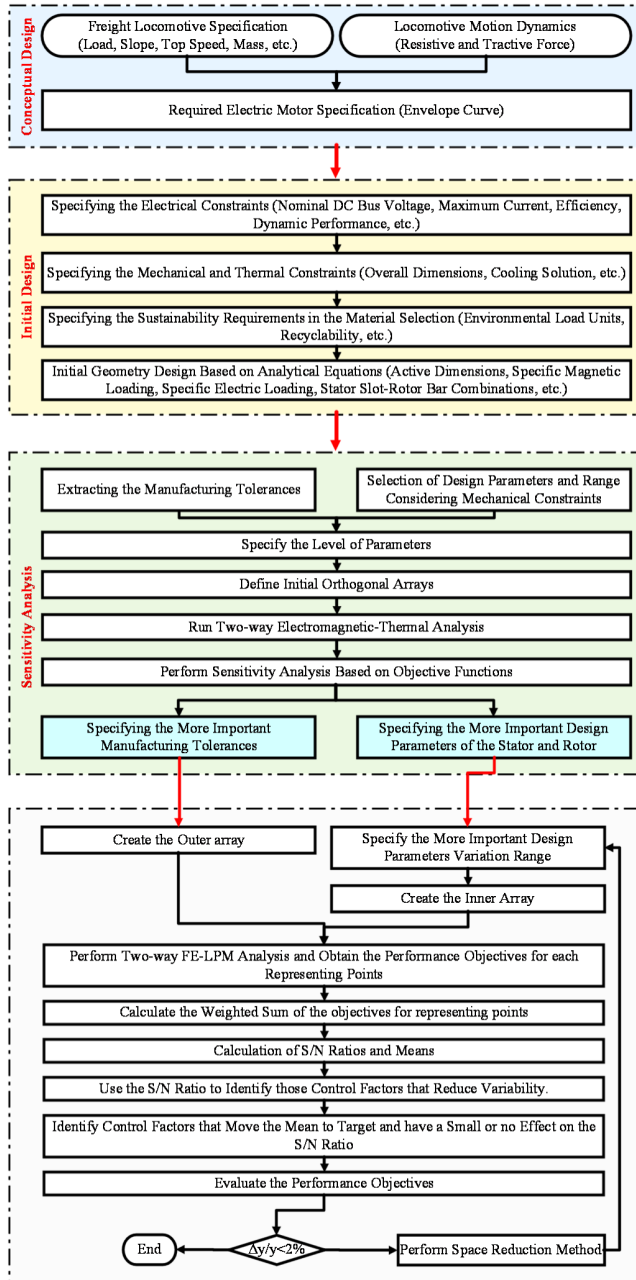
FIGURE 5. The proposed robust optimization algorithm.

2) ALUMINIUM COMPRESSED COILS

In the production process of aluminum cage, the diecast process can be used with high economic efficiency to make the rotor cage, due to the low melting temperature of aluminum. The stator will consist of compressed windings. Therefore, the stator should be manufactured in several pieces, increasing the manufacturing complexity.

C. ENVELOPE CURVE

The torque/power-speed curves of the upgraded motors are shown in Fig. 4, created using multi-physics analysis considering the following parameters:
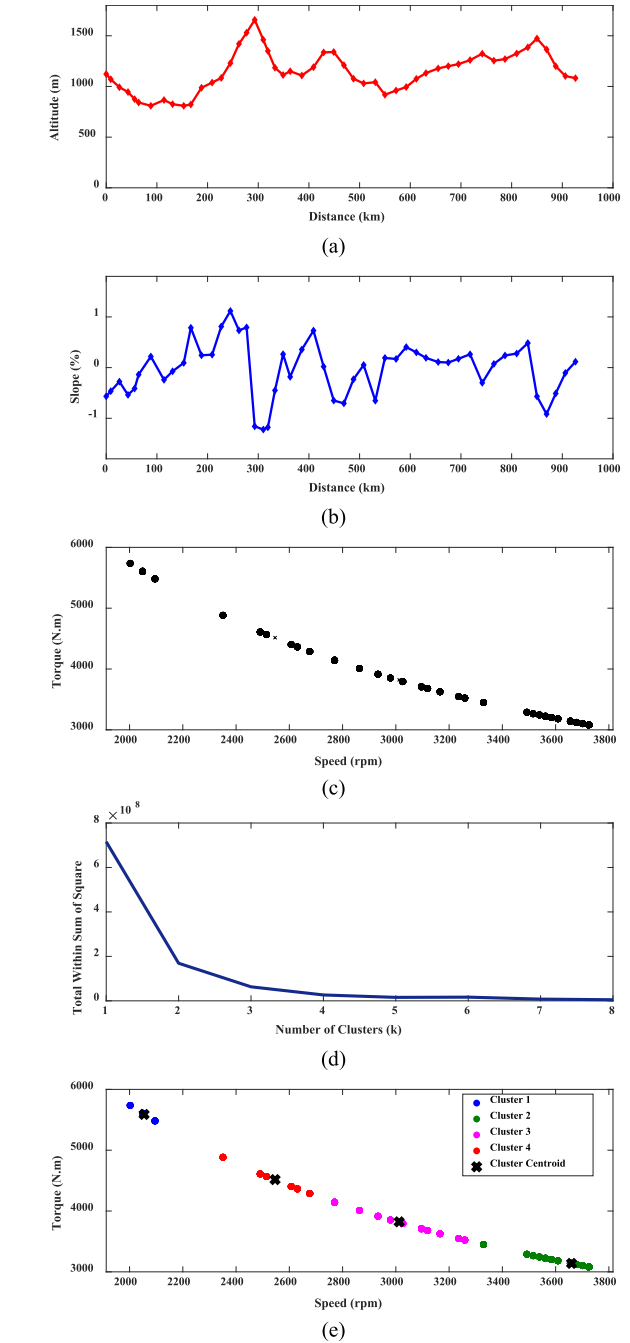

FIGURE 6. (a) The variation of altitudes of the train stations regarding to distance of the starting point (Tehran), (b) The calculated average slope of the train stations, (c) The working points of the EFL, (d) The optimum number of k-means clusters and (e) the detail of the clusters and representing points.

TABLE 3. The details of the representing points.

Cluster Number	Speed (rpm)	Torque (Nm.)	Cluster Weight
1	2055	5590	57
2	3660	3140	586
3	3013	3824	178
4	2547	4518	106

1. A winding hotspot temperature of 155°C.

2. The switching type is Sine/triangle with 3rd harmonic injection

3. The corresponding DC link voltage to the selected switching method is 2685 V.

4. The maximum current limit is 800 A.

The results indicate that both improved traction motors completely cover the torque-speed curve of the required traction motor and meet the requirements of the EFL.

IV. ROBUST OPTIMIZATION DESIGN

This section presents the systematic robust design procedure of an IM for EFL applications. The proposed robust optimization algorithm is shown in Fig. 5. The details of the proposed multi-physics robust design are as follows.

A. EXTRACTING THE WORKING MODES OF THE EFL

Generally, the EFL is designed to work for a specific route. In this paper a rail route of Tehran-Mashhad is considered as a case study. From Tehran to Mashhad there are 50 train stations. To calculate the gravity resistance effort between two stations, it is necessary to calculate the slope of the route. In this study the average slope between two stations is considered. The slope (α) of the route is calculated based on the difference between the altitudes (height above mean sea level) of two consequent train stations. The variation of altitudes of the train stations regarding to distance of the starting point (Tehran) is shown in Fig. 6 (a) and the corresponded calculated slopes values are illustrated in Fig. 6 (b). By intersection of locomotive tractive effort and load lines curves corresponding to each station's average slope, the working points of the EFL for this route are calculated and presented in Fig. 6 (c).

To optimize the performance of the traction motor, it challenging to consider all working points due to the resultant high computational time. Instead, it is better to obtain representative points. In this paper, the K-means clustering method is utilized to obtain the representing points. The k-means method is an unsupervised machine learning method that clusters a set of data into a specific number (k) of a cluster. K-means is a method of vector quantification that is originally derived from signal processing and is popular for data analysis in data mining [30]. Given a set of observations $(x_1, x_2, \ldots, x_n)$ in which each observation is a d-dimensional vector. The purpose of K-means is to cluster n observations into $k \leq n$ sets $S = \{S_1, S_2, \ldots, S_k\}$. So that the sum of the squares of the difference from the mean (i.e., variance) for each cluster is minimized [31]. The exact mathematical definition is as Eq. 8.

$$\arg\min_{S} \sum_{i=1}^{k} \sum_{x \in S_i} \|x - \mu_i\|^2 = \arg\min_{S} \sum_{i=1}^{k} |S_i| \, Var(S_i) \quad (8)$$

where μ_i is the mean of the points in S_i. This is equivalent to minimizing squares of deviations from points in the same cluster. This method requires the user to specify the number of clusters as the input of the algorithm. To get the right number of clusters, it is necessary to use methods such as Elbow, Silhouette and Gap Statistics.

The Elbow method is used to calculate the optimum number of clusters. In this method, the sum of the squares of the distance between the data in each cluster and the center of that cluster is calculated as the Distortion criterion. Once this criterion is plotted for the entire number of clusters, it is possible to visually determine the best value of k. The obtained shape is like an ''arm''. So, the knee point represents the best value of k. Using the Elbow method, the effect of the number of clusters on the sum of the deviation squares is shown in Fig. 6 (d). Considering more than 4 clusters is shown not to have much effect on increasing accuracy. Therefore, the optimal number of clusters is 4. By applying the k-means method to the motor working points in the specified route, the representing points are calculated. The results are shown in Fig. 6 (e) and Table 3.

B. DEFINE OBJECTIVE FUNCTIONS

The aim of this study is to evaluate the capability of aluminum-based and copper-based IMs for the given EFL considering manufacturing tolerances.

C. EXTRACTING THE MANUFACTURING TOLERANCES

Manufacturing of electrical machines is subject to tolerances and uncertainties at every stage of fabrication and assembly. Air gap length is here selected as the manufacturing tolerance to be considered in the optimization process.

D. SENSITIVITY ANALYSIS

To minimize computation time, it is necessary to identify and eliminate the less important parameters and manufacturing tolerances in the optimization process. The signal to noise ratio, local SA, global SA, design equation, and correlation coefficient are commonly used to identify the effect of parameters on objective functions [32]. The SA methods based on Design of Experiments (DOE) are the most favorable ones. DOE is a statistical method for analysis of experimental results. The most crucial feature of DOE is an arrangement of the small number of experiments for data analysis. Partial factor design is carried out using Orthogonal Array (OA) [33]. The OAs are predefined tables that the rows present the combination of design variables, and the objective values are presented in the column; the columns of the arrays are balanced and orthogonal. This means that in each pair of columns, all factor combinations occur the same number of times. Orthogonal designs estimate the effect of each factor on the objectives independently of all other factors [34].

1) GEOMETRY AND COOLING SOLUTION PARAMETERS

In this paper 13, geometry and cooling solution parameters are considered. Six of them are related to stator part including stator tooth width (TW_s), stator slot depth (SD_s), stator tooth tip depth (TTD_s), stator slot opening (SO_s), stator cooling duct ratio (CDR_s), and stator duct gap (DG_s). The remaining seven parameters are related to rotor including bar opening width (just for copper-based design) (BOW_r), bar opening depth

TABLE 4. The considered oa for SA of the aluminum-based design L27(2^{12}).

| Run	TW_s	SD_s	TTD_s	SO_s	CDR_s	DG_s	BOD_r	TW_r	BD_r	Ag	IRD_r	RDR_r	T_w	T_{ave}	PF	Eff	$f(x)$
1	13.5	46.55	1.8	9	0.315	4.5	1.8	18.495	22.14	1.8	252	18	111	7045	0.81	95.56	1.004161
2	13.5	46.55	1.8	9	0.35	5	2	20.55	24.6	2	280	20	112	7047	0.82	95.54	1.003978
:	:	:	:	:	:	:	:	:	:	:	:	:	:	:	:	:	:
12	15	46.55	2	11	0.385	4.5	2	22.605	22.14	2	308	18	107	7075	0.852	95.1	0.98866
13	15	51.73	2.2	9	0.315	5	2.2	20.55	27.06	1.8	308	18	108	7033	0.826	95.6	0.995183
:	:	:	:	:	:	:	:	:	:	:	:	:	:	:	:	:	:
26	16.5	56.9	2	9	0.35	4.5	2.2	18.495	27.06	2	308	20	117	7030	0.786	95.5	1.022039
27	16.5	56.9	2	9	0.385	5	1.8	20.55	22.14	2.2	252	22	119	7061	0.809	95	1.020788
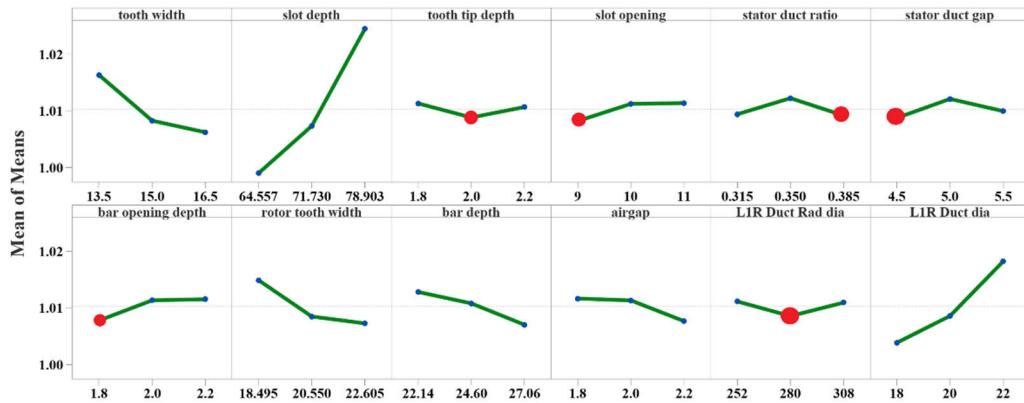
FIGURE 7. The calculated mean values of aluminium-based design.

(BOD_r), rotor tooth width (TW_r), bar depth (BD_r), airgap (Ag), rotor inner duct diameter (IRD_r), the rotor duct radius (RDR_r).

2) CALCULATION METHOD

For 13 variables and three levels for each variable, in the case of full factorial design, the required FEM samples are $3^{13} = 1594323$ whereas to perform the SA using OA, only 27 FEM runs are required. For SA, the considered levels are (1-10%) x_i, x_i, and (1+10%) x_i. Where x_i is the value of the initial design. The summary details of OA of geometry and cooling solution parameters are shown in Table 4. The considered OAs for copper-based and aluminum-based designs are $L_{27}(3^{13})$ and $L_{27}(3^{12})$, respectively.

In this paper, the weighted sum approach is used to implement the Multi Objective (MO) SA. The combination of the weighted sum approach and MO Taguchi optimization method is applied to identify essential parameters on objectives. The weighted sum of the objectives defined as Eq. 9. All the three terms have the same weight factor of $\omega_1 = \omega_2 = \omega_3 = 0.333$. The implemented procedure is as follows:

1. Calculating the objective function for all 27 runs, according to Eq. 9.
2. Calculate the S/N ratio for each row in Table 4.
3. Compute the S/N ratio for each level of factors using Eq. 10 (with a target as smaller is better).
4. Specifying the importance degree of each design variable using Minitab software.

TABLE 5. Optimization variables and ranges.

Parameter	Unit	Range
tooth width	mm	[12, 18]
slot depth	mm	[41.4, 62.08]
rotor tooth width	mm	[16.44, 24.66]
bar depth	mm	[19.68, 29.52]
airgap	mm	[1.6, 2.4]
L1R Duct diameter	mm	[16, 24]

$$min : f(x) = \omega_1 \frac{T_{ave}(initial)}{T_{ave}(i)} + \omega_2 \frac{Eff(initial)}{Eff(i)}$$
$$+ \omega_3 \frac{PF(initial)}{PF(i)} + \omega_4 \frac{T_w(i)}{T_w(initial)} \quad (9)$$

$$S/N = -10\log\left(\sum_{i=1}^{n} \frac{y_i^2}{l}\right) \quad (10)$$

where l is the number of repeats in each experiment, and y_i is the output of the experiment in i^{th} repeat.

3) RESULTS

For the aluminum-based design the importance degree of the parameters is $SD_s > RDR_r > TW_s > TW_r > BD_r > Ag > BOD_r > DG_s > SO_s > CDR_s > IRD_r > TTD_s$.

An interesting result of SA is the importance rank of the rotor duct radius (RDR_r). To determine the reason behind this, thermal analysis is carried out for two radiuses of 18 and 22 mm and the passing flow rates of rotor ducts, stator ducts, and airgap are calculated. The results indicate that with increasing radius the flow rates of rotor ducts, stator ducts,

TABLE 6. The inner and outer array of the robust design $L_{25}(5^6)$.

Run	Inner Array						Outer Array			
							Aluminum-based		Copper-Based	
	TW_s	SD_s	TW_r	BD_r	Ag	RDR_r	$F_{T,AL}(1)$	$F_{T,AL}(2)$	$F_{T,CU}(1)$	$F_{T,CU}(2)$
1	1	1	1	1	1	1	0.965234	0.949785	1.000161	0.950508
2	1	2	2	2	2	2	0.960595	0.945172	0.971681	0.946637
⋮	⋮	⋮	⋮	⋮	⋮	⋮	⋮	⋮	⋮	⋮
12	3	2	4	1	3	5	0.995983	0.958626	0.992333	0.96112
13	3	3	5	2	4	1	0.982258	0.948514	0.990803	0.949984
⋮	⋮	⋮	⋮	⋮	⋮	⋮	⋮	⋮	⋮	⋮
24	5	4	3	2	1	5	1.033701	0.963654	1.029354	0.970186
25	5	5	4	3	2	1	1.005377	0.950921	0.991215	0.955236

and airgap change from 0.517, 2.699, and 0.7841 m^3/s to 0.3749, 3.046, and 0.5792 m^3/s, respectively. Therefore, with increasing the RDR_r, the cooling flow ratios of stator and airgap are reduced and consequently the winding temperature is increased. Therefore, six parameters of SD_s, RDR_r, TW_s, TW_r, BD_r, Ag are considered as the more important design parameters. The less important design parameters are set at their optimum values.

For the copper-based design, the importance degree of the parameters is $SD_s > RDR_r > TW_s > TW_r > BD_r > Ag > BOD_r > DG_s > SO_s > CDR_s > BOW_r > IRD_r > TTD_s$. Therefore, the first six parameters are considered as the more important design parameters.

For both the copper and aluminum designs, the less important design parameters are set at their optimum values.

E. OPTIMIZE THE LESS-IMPORTANT DESIGN PARAMETERS

The two-level Taguchi optimization method is applied to obtain the best combination of the design parameters. The goal of a two-level optimization is to obtain a parameter combination that can minimize the variability of the objective about some ideal geometry parameter. The first step concentrates on minimizing variability, and the second focuses on hitting the target as illustrated in Fig. 7. Adjusting the level of one or more parameters that substantially affects the mean but not the S/N to put the objective on target. According to Fig. 7, for the aluminum-based design, the optimum level of less important design parameters is tooth tip depth (level 2), slot opening (level 1), stator duct ratio (level 3), stator duct gap (level 1), bar opening depth (level 1), L1R Duct Rad diameter (level 2).

F. ROBUST OPTIMIZATION METHOD TO OPTIMIZE THE MORE IMPORTANT DESIGN PARAMETERS

1) IMPLEMENTATION OF THE TAGUCHI METHOD

To implement the robust design using the Taguchi method, two OAs are needed. The first OA (known as an inner array) includes the more important design parameters, and the second OA (known as an outer array) includes the manufacturing tolerances. Six design parameters of SD_s, RDR_r, TW_s, TW_r, BD_r, Ag (with five levels of (1-20%) x_i, (1-10%) x_i, x_i,

(1+10%) x_i, and (1+20%) x_i) and one manufacturing tolerances of airgap length (with two levels of $-\Delta A_g$ and $+\Delta A_g$) are considered. The variation range of design parameters are presented in Table 5 and the manufacturing tolerance is set as 0.02 mm.

The FEM runs required to implement the robust design are shown in Table 6. The overall objective function of each parameter combination is calculated by averaging the calculated objective functions of the outer array. For example, the overall objective function of the aluminum-based design for first design parameters combination (RUN #1) is calculated by averaging the values of $F_{T,AL}(1)$ and $F_{T,AL}(2)$. In the optimization procedure, three constraints of stator winding current density (J_c), stator winding hotspot temperature ($T_{winding\_hotspot}$), and stator slot fill factor (sf) are considered in Eq. 11. To integrate these constraints into the Taguchi method, a penalty objective function of ($y_{i,j}$) is defined in Eq. 12.

$$g_1(x): J_c \leq 6\frac{A}{mm^2})$$
$$g_2(x): T_{winding\_hotspot} \leq 155°C$$
$$g_3(x): sf \begin{cases} 0.5 & conventional\ CU - based\ design \\ 0.67 & compressed\ AL - based\ design \end{cases}$$
$$(11)$$

$$y_{i,j} = f(x_{i,j}) + 1000 \sum_{k=1}^{K} u(g_{i,j}) \quad (12)$$

where i (ranging from 1 to the size of inner array = 25), j (ranging from 1 to the size of outer array = 2), and K are the indices of the design parameters combinations, manufacturing tolerances levels, and the number of optimization constraints, respectively, as shown in Table 6. If any of the specified constraints in Eq. 11 is violated, the value of $u(g_{i,j})$ is designated as 1; otherwise, it is set to 0. For example, for aluminum-based design, $f(x_{25,2})$ denotes the calculated objective functions for RUN #25 within the inner array of Table 6, corresponding to level 2 of the outer array (i.e., $F_{T,AL}(2)$).

2) SPACE REDUCTION METHOD

One of the drawbacks of the Taguchi method is the limited levels of parameter variation. To improve the Taguchi
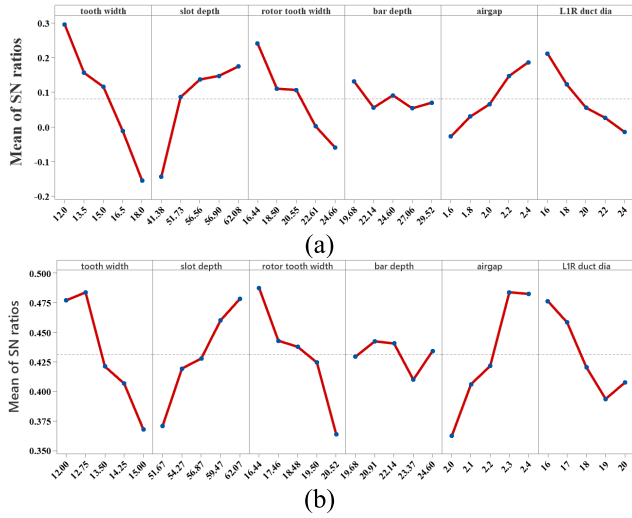
FIGURE 8. The obtained S/N ratios of different levels of the aluminium-based design. (a) Iteration 1 and (b) Iteration 2.
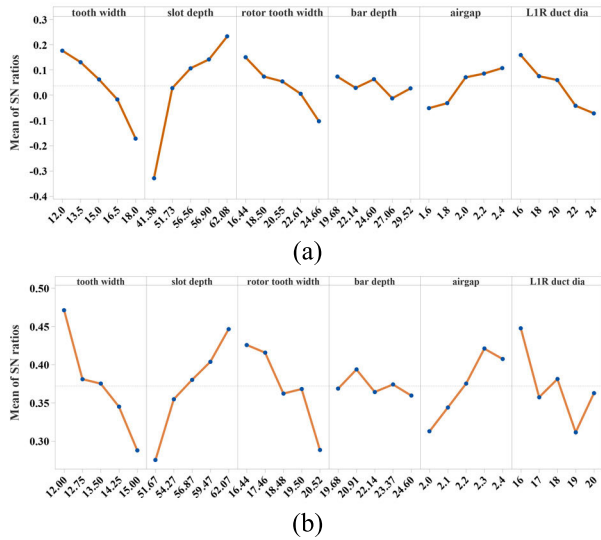

FIGURE 9. The obtained S/N ratios of different levels of the copper-based design. (a) Iteration 1 and (b) Iteration 2.

method, space reduction methods can be utilized. Therefore, in a multi-level optimization procedure, the variation ranges of the design parameters are modified at each level. For example, considering the allowable variation range of the design parameter [a, b] and five levels for each parameter, if the optimum value of the Taguchi is equal to x_t, the new variation range of the parameter A is as Eq. 13.

$$\begin{cases} (a, a+d_i, a+2d_i, a+3d_i, a+4d_i) & x_t-2d_i < a \\ (b-4d_i, b-3d_i, b-2d_i, b-d_i, b) & x_t+2d_i > b \\ (x_t-2d_i, x_t-d_i, x_t, x_t+d_i, x_t+2d_i) & others \end{cases}$$

(13)

where d_i is the distance between two levels (the initial step size is 10% initial value). In each step of the utilized multi-level optimization procedure, the value of step size is halved.

TABLE 7. Levels of optimization variables at each iteration of the aluminum-based design.

Iteration	Level	TW_s	SD_s	TW_r	BD_r	Ag	RDR_r
1	1	**12**	41.384	**16.44**	**19.68**	1.6	**16**
	2	13.5	46.55	18.49	22.14	1.8	18
	3	15	51.73	20.55	24.6	2	20
	4	16.5	56.90	22.60	27.06	2.2	22
	5	18	**62.07**	24.66	29.52	**2.4**	24
2	1	12	51.67	**16.44**	19.68	2	**16**
	2	**12.75**	54.27	17.46	**20.91**	2.1	17
	3	13.5	56.87	18.48	22.14	2.2	18
	4	14.25	59.47	19.5	23.37	**2.3**	19
	5	15	**62.07**	20.52	24.6	2.4	20

TABLE 8. Levels of optimization variables at each iteration of the copper-based design.

Iteration	Level	TW_s	SD_s	TW_r	BD_r	Ag	RDR_r
1	1	**12**	41.384	**16.44**	**19.68**	1.6	**16**
	2	13.5	46.55	18.49	22.14	1.8	18
	3	15	51.73	20.55	24.6	2	20
	4	16.5	56.90	22.60	27.06	2.2	22
	5	18	**62.07**	24.66	29.52	**2.4**	24
2	1	**12**	51.67	**16.44**	19.68	2	**16**
	2	12.75	54.27	17.46	**20.91**	2.1	17
	3	13.5	56.87	18.48	22.14	2.2	18
	4	14.25	59.47	19.5	23.37	**2.3**	19
	5	**15**	**62.07**	20.52	24.6	2.4	20

The multi-level optimization procedure is continued until the difference between the calculated objective function of the k+1 and k levels are lower than $\varepsilon = 1\%$.

G. RESULTS
The results of S/N ratios for each iteration of aluminum and copper-based designs are presented in Fig. 8 and 9, respectively. Also, the defined parameters levels of each iteration for aluminum-based and copper-based designs are presented in Table 7 and 8, respectively. The average S/N ratio of a level of a parameter can be calculated based on Eq. 10 and Table 6. For example, to calculate the average S/N ratio for the first level of the SD_s consider the second column of Table 6. The average S/N ratio corresponding to level one is calculated by averaging as Eq. 14.

$$\overline{S/N}(SD_s, 1)$$
$$= \frac{S/N(1)+S/N(6)+S/N(11)+S/N(16)+S/N(21)}{5(Number\ of\ levels)}$$

(14)

The best design level of each optimization variable corresponds to the level with the highest S/N ratio. For instance, in iteration 1 of the aluminum-based design, the optimum level of the TW_s and SD_s are level 1(corresponding to 12 mm) and level 5 (corresponding to 62.07 mm), respectively.

The optimum level of each parameter is bolded in Table 7 and 8. After obtaining the optimum levels of iteration 1, it is necessary to use Eq. 13 to reduce the design parameters variation range and halve the step size. For example, in iteration
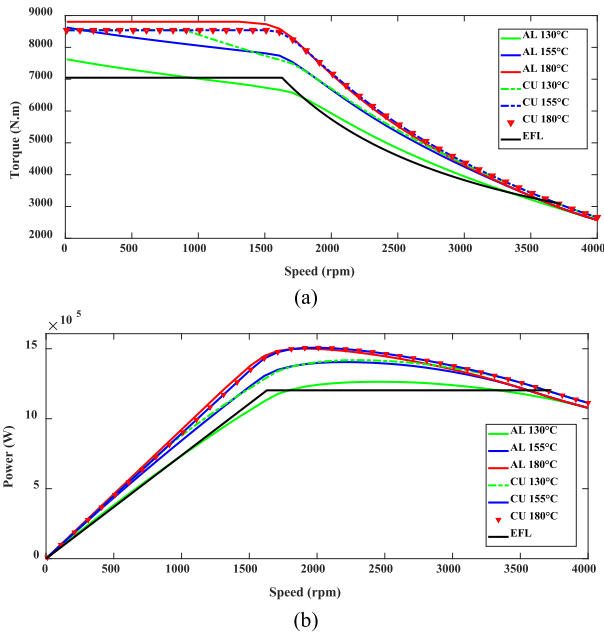
FIGURE 10. The performance comparison of optimum designs and EFL requirements (a) torque-speed and (b) power-speed.
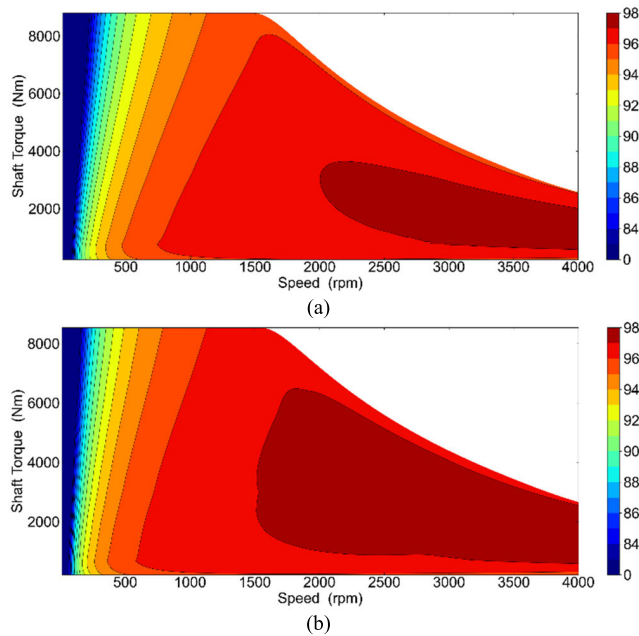

FIGURE 11. The efficiency map of optimum designs (a) Aluminium and (b) Copper.
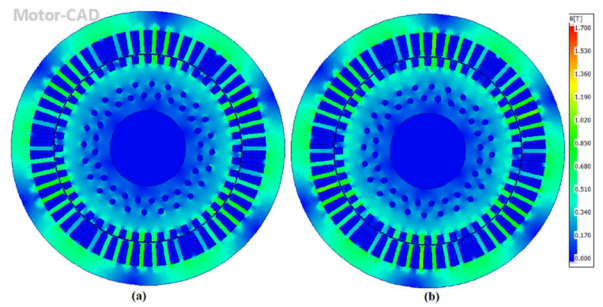

FIGURE 12. The magnetic flux density of optimum designs (a) Aluminium and (b) Copper.
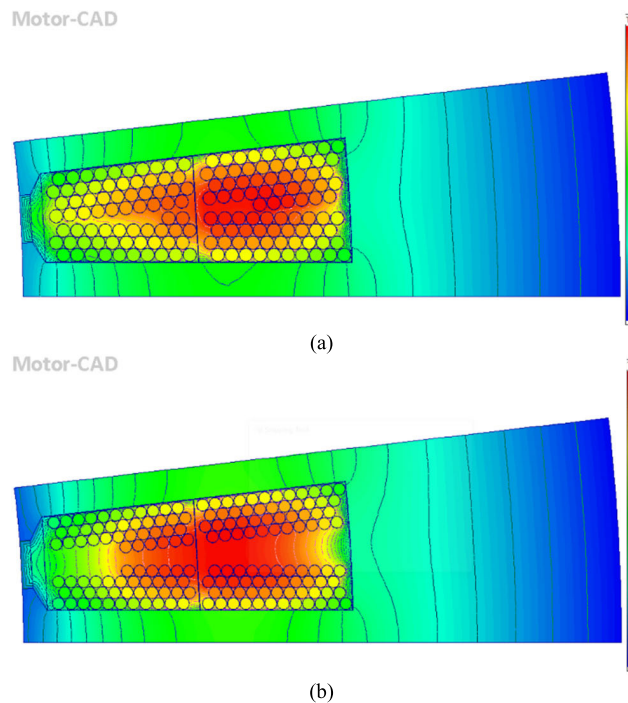
FIGURE 13. The temperature distribution of optimum designs (a) Aluminium and (b) Copper.

2, the step size of parameter TW_s is reduced from 1.5 mm to 0.75 mm.

Both aluminum and copper-based designs converge after two iterations. From Fig. 9 and 10, it is evident that the S/N ratios for all optimization variables in each iteration have shown significant improvement, accompanied by a noteworthy reduction in the variation ranges of the S/N ratios. The S/N ratio serves as a metric that compares the level of a desired signal to the level of background noise. It is defined

as the ratio of signal power to noise power, often expressed in decibels. A ratio higher than 1:1 (greater than 0 dB) indicates a prevalence of signal over noise.

In the second iteration of the optimization procedure, the calculated values of the S/N ratios for all parameter levels exhibit a positive sign, with the amplitude of the S/N ratio hovering around 0.4 dB. These results suggest not only an improvement in the performance characteristics of the modified design but also an increase in the robustness of the designed motor against manufacturing tolerances.

H. PERFORMANCE COMPARISON OF COPPER-BASED AND ALUMINIUM-BASED DESIGNS
1) ENVELOPE CURVE
Generally, a temperature sensor is mounted on the end windings of traction motors to help control over-temperature issues to prevent short circuits or other winding damage.

A fault in the windings of traction motors can interrupt locomotive function, leading to significant financial problems. Additionally, repairing and replacing these windings demands a considerable amount of time and money. Therefore, operating traction motors at lower working temperatures can significantly increase their lifetime and reliability. On the other hand, the manufacturing processes of electrical machines can negatively impact the efficiency and performance of the electric machines, and it may be challenging to reach an agreement between the FEM simulation and experimental results [35]. Considering these factors, a safe margin between the capability curve obtained through FEM simulations and the required curve for actual operation is crucial during the FEM simulation and design process of electrical machines. To evaluate the envelope curves of optimum designs, two-way electromagnetic thermal designs for different levels of limited hotspot temperature are carried out. In Fig. 10, the effect of hotspot temperature on the envelope curve of the designed traction motors is investigated. Based on the obtained results, the designed traction motors can completely satisfy the requirements of EFL applications, and their capability curves have a reasonable safety margin. The results also indicate that for the copper-based design, the limitation value of 130°C can be defined, while for the aluminum-based design, a higher limit (for instance, 155°C) should be considered.

2) EFFICIENCY MAP

The efficiency maps of the aluminum-based and copper-based optimum designs with considering the maximum current of 800A are illustrated in Fig. 11 (a) and (b), respectively. The copper-based design has a wider more efficient region compared to aluminum-based. For example, in the copper-based design the most-efficient region starts from a speed of 1500 rpm and torque of 6000 Nm compared to a speed of 2000 rpm and torque of 4000 Nm for the aluminum version.

The efficiency difference of the two motors over the drive cycle, $\eta(AL - CU)$, can be calculated using the weighted 4 representative points of table 3 and Eq. 15. In this equation, ω_c is the cluster weights of the representing points and k is the number of clusters. η_{c-AL} and η_{c-CU} are the efficiency of the aluminum and copper machines, respectively. The results indicate that over the considered driving cycle, the weighted efficiency of the machines is 0.989. Therefore, the copper design efficiency over driving cycle is 1.1% higher than aluminum design.

$$\eta(AL - CU) = \frac{\sum_{i=1}^{k} \omega_c(i) \times \eta_{c-AL}(i)}{\sum_{i=1}^{k} \omega_c(i) \times \eta_{c-CU}(i)} \quad (15)$$

3) MAGNETIC FLUX DENSITY

The magnetic flux density distribution of the optimum aluminum and copper-based designs at operating points of 3660 rpm and 3140 Nm are illustrated in Fig. 12 (a) and (b),

respectively. In both designs the magnetic flux density of tooth is about 1.1 T and oversaturation does not occur.

4) FEM TEMPERATURE DISTRIBUTION

To have a better insight into the working temperature condition of the designed IMs, the FEM temperature distribution of the optimum aluminum and copper-based designs at operating point of 3660 rpm and 3140 N.m are illustrated in Fig. 13 (a) and (b), respectively. As expected, the working temperature of the copper-based design is 16°C lower than aluminum-based. The results indicate that the strands closer to airgap have a lower temperature due to air cooling flow of the airgap.

I. COMPARISON OF COMPUTATIONAL TIME

In terms of computational time, numerous FEM runs will be needed to implement robust optimization of electric machines over the driving cycle using conventional optimization techniques. Using various strategies and tactics, the suggested algorithm in this article has significantly decreased the number of necessary FEM runs. First, using SA, parameters that are more important were found, reducing the number of calculations by allowing only these parameters to be optimized. In the stage of SA, the number of design parameters for copper-based and aluminum-based designs are 13 and 12, respectively. Therefore, in the case of full factorial design, the required FEM samples for copper-based and aluminum-based designs are $3^{13} = 1594323$ and $3^{12} = 531441$, respectively. Whereas to perform the SA using OA, only 27 FEM runs are required. Conversely, the optimization operating points were significantly reduced by using the representing points. The K-means clustering method with the Elbow method's criteria selection was chosen from among the various approaches. Additional representing points are needed for other approaches, such as the Energy Centre of Gravity or the Geometrical Centre of Gravity, which increases the number of FEM runs [36]. Lastly, robust optimization was implemented using the Taguchi method. With a relatively small number of simulations, this method yields the best combination of design parameters and is easily implemented in statistical software. The quantity of simulations needed would significantly rise if evolutionary processing techniques like artificial neural networks, kriging models, etc. were utilized [37]. In comparison to alternative methods, the suggested algorithm and the methods chosen for each optimization step have reduced computational time, memory requirements, and implementation complexity overall. The efficiency of the suggested optimization algorithm was such that the correct results could only be obtained with a two-way electromagnetic-thermal FEM simulation $27 + 2 \times 4 \times 25 \times 2 = 427$ (SA + Optimization Level × Number of Clusters × Inner Array × Outer Array).

V. CONCLUSION

A design process of the traction motor for Electric Freight Locomotive was developed to obtain a systematic

multi-physics robust design over a real driving cycle, considering the geometry parameters, guiding tractive equations, and cooling system. The proposed optimization algorithm considered manufacturing uncertainties and has been utilized to design a copper wound and aluminum wound IM, both with a continuous power of 1203 kW.

The comparative study of aluminum-based and copper-based design is carried out to evaluate the effectiveness of proposed sequential multi-physics and multi-operation mode robust optimization procedure. The obtained results indicate that in addition to enhancement in performance characteristics of the modified design, the robustness of the designed motor against manufacturing tolerances was increased too. Also, it shown that that the compressed winding aluminum-based design is capable of completely fulfilling the requirements of the EFL applications. However, compared to copper-based design the aluminum version has lower efficiency, higher winding working temperature and lower safe margin based on the FEM-based envelope curve.

REFERENCES

[1] S. Nategh, A. Boglietti, Y. Liu, D. Barber, R. Brammer, D. Lindberg, and O. Aglen, "A review on different aspects of traction motor design for railway applications," *IEEE Trans. Ind. Appl.*, vol. 56, no. 3, pp. 2148–2157, May 2020, doi: 10.1109/TIA.2020.2968414.

[2] B. Ma, J. Zheng, J. Zhu, J. Wu, G. Lei, and Y. Guo, "Robust design optimization of electrical machines considering hybrid random and interval uncertainties," *IEEE Trans. Energy Convers.*, vol. 35, no. 4, pp. 1815–1824, Dec. 2020, doi: 10.1109/TEC.2020.2996244.

[3] Y. Yang, C. Zhang, G. Bramerdorfer, N. Bianchi, J. Qu, J. Zhao, and S. Zhang, "A computationally efficient surrogate model based robust optimization for permanent magnet synchronous machines," *IEEE Trans. Energy Convers.*, vol. 37, no. 3, pp. 1520–1532, Sep. 2022, doi: 10.1109/TEC.2021.3140096.

[4] Z. Shi, X. Sun, Y. Cai, and Z. Yang, "Robust design optimization of a five-phase PM hub motor for fault-tolerant operation based on Taguchi method," *IEEE Trans. Energy Convers.*, vol. 35, no. 4, pp. 2036–2044, Dec. 2020, doi: 10.1109/TEC.2020.2989438.

[5] K. Kim and B. Lee, "Taguchi's robust design optimisation of water-cooled ISG motors considering manufacturing tolerances," *IET Electric Power Appl.*, vol. 14, no. 5, pp. 865–871, May 2020, doi: 10.1049/iet-epa.2019.0574.

[6] J. D. Widmer, R. Martin, and M. Kimiabeigi, "Electric vehicle traction motors without rare Earth magnets," *Sustain. Mater. Technol.*, vol. 3, pp. 7–13, Apr. 2015, doi: 10.1016/j.susmat.2015.02.001.

[7] T. Wang, P. Zheng, Q. Zhang, and S. Cheng, "Design characteristics of the induction motor used for hybrid electric vehicle," *IEEE Trans. Magn.*, vol. 41, no. 1, pp. 505–508, Jan. 2005, doi: 10.1109/TMAG.2004.838967.

[8] M. J. Akhtar and R. K. Behera, "Optimal design of stator and rotor slot of induction motor for electric vehicle applications," *IET Electr. Syst. Transp.*, vol. 9, no. 1, pp. 35–43, Mar. 2019, doi: 10.1049/iet-est.2018.5050.

[9] M. Tumbek, Y. Oner, and S. Kesler, "Optimal design of induction motor with multi-parameter by FEM method," in *Proc. 9th Int. Conf. Electr. Electron. Eng. (ELECO)*, Nov. 2015, pp. 1053–1056, doi: 10.1109/ELECO.2015.7394483.

[10] H. Apaydın, O. Kara, and N. F. O. Serteller, "Investigation of the efficiency improvement on a 1.1 kW three-phase asynchronous motor," *Turkish J. Electromechanics Energy*, vol. 7, no. 2, pp. 58–66, Oct. 2022. Accessed: Feb. 20, 2024. [Online]. Available: https://www.scienceliterature.com/index.php/TJOEE/article/view/230

[11] B. Dianati, S. Kahourzade, and A. Mahmoudi, "Optimization of axial-flux induction motors for the application of electric vehicles considering driving cycles," *IEEE Trans. Energy Convers.*, vol. 35, no. 3, pp. 1522–1533, Sep. 2020, doi: 10.1109/TEC.2020.2976625.

[12] E. Roshandel, A. Mahmoudi, W. L. Soong, and S. Kahourzade, "Optimal design of induction motors over driving cycles for electric vehicles," *IEEE Trans. Veh. Technol.*, vol. 72, no. 12, pp. 15548–15562, Dec. 2023, doi: 10.1109/TVT.2023.3292901.

[13] N. Riviére, M. Villani, and M. Popescu, "Optimisation of a high speed copper rotor induction motor for a traction application," in *Proc. IECON 45th Annu. Conf. IEEE Ind. Electron. Soc.*, vol. 1, Oct. 2019, pp. 2720–2725, doi: 10.1109/IECON.2019.8927627.

[14] F. Mahmouditabar and N. J. Baker, "Design optimization of induction motors with different stator slot rotor bar combinations considering drive cycle," *Energies*, vol. 17, no. 1, p. 154, Dec. 2023, doi: 10.3390/en17010154.

[15] M. Popescu, L. Di Leonardo, G. Fabri, G. Volpe, N. Riviere, and M. Villani, "Design of induction motors with flat wires and copper rotor for E-Vehicles traction system," *IEEE Trans. Ind. Appl.*, vol. 59, no. 3, pp. 3889–3900, May 2023, doi: 10.1109/TIA.2023.3256391.

[16] T.-V. Tran, E. Nègre, K. Mikati, P. Pellerey, and B. Assaad, "Optimal design of TEFC induction machine and experimental prototype testing for city battery electric vehicle," *IEEE Trans. Ind. Appl.*, vol. 56, no. 1, pp. 635–643, Jan. 2020, doi: 10.1109/TIA.2019.2943447.

[17] F. Mahmouditabar, A. Vahedi, and N. Takorabet, "Robust design of BLDC motor considering driving cycle," *IEEE Trans. Transport. Electrific.*, early access, Jun. 21, 2023, doi: 10.1109/TTE.2023.3285650.

[18] G. Lei, G. Bramerdorfer, C. Liu, Y. Guo, and J. Zhu, "Robust design optimization of electrical machines: A comparative study and space reduction strategy," *IEEE Trans. Energy Convers.*, vol. 36, no. 1, pp. 300–313, Mar. 2021, doi: 10.1109/TEC.2020.2999482.

[19] G. Lei, G. Bramerdorfer, B. Ma, Y. Guo, and J. Zhu, "Robust design optimization of electrical machines: multi-objective approach," *IEEE Trans. Energy Convers.*, vol. 36, no. 1, pp. 390–401, Mar. 2021, doi: 10.1109/TEC.2020.3003050.

[20] V. Rafiee and J. Faiz, "Robust design of an outer rotor permanent magnet motor through six-sigma methodology using response surface surrogate model," *IEEE Trans. Magn.*, vol. 55, no. 10, pp. 1–10, Oct. 2019, doi: 10.1109/TMAG.2019.2923160.

[21] K. Diao, X. Sun, G. Lei, G. Bramerdorfer, Y. Guo, and J. Zhu, "Robust design optimization of switched reluctance motor drive systems based on system-level sequential Taguchi method," *IEEE Trans. Energy Convers.*, vol. 36, no. 4, pp. 3199–3207, Dec. 2021, doi: 10.1109/TEC.2021.3085668.

[22] J. Wu, X. Zhu, Z. Xiang, D. Fan, L. Quan, and L. Xu, "Robust optimization of a rare-earth-reduced high-torque-density PM motor for electric vehicles based on parameter sensitivity region," *IEEE Trans. Veh. Technol.*, vol. 71, no. 10, pp. 10269–10279, Oct. 2022, doi: 10.1109/TVT.2022.3183503.

[23] J.-C. Son, J.-Y. Kim, J.-W. Choi, D.-K. Lim, and H.-K. Yeo, "Performance enhancement of the IPMSM for HEV applications using grain-oriented electrical steel and design optimization," *IEEE Access*, vol. 10, pp. 46599–46607, 2022, doi: 10.1109/ACCESS.2022.3170896.

[24] M. Ehsani, Y. Gao, and A. Emadi, "Modern electric, hybrid electric, and fuel cell vechicles: Fundamentals, theory, and design," in *Modern Electric, Hybrid Electric, and Fuel Cell Vechicles: Fundamentals, Theory, and Design*, 2nd ed. Boca Raton, FL, USA: CRC Press, Jan. 2017, pp. 1–535, doi: 10.1201/9781420054002.

[25] *The Tractive Resistance of Electric Locomotives and Cars | WorldCat.org*. Accessed: Apr. 3, 2023. [Online]. Available: https://www.worldcat.org/title/tractive-resistance-of-electric-locomotives-and-cars/oclc/7770840

[26] Z. Yuan, M. Wu, C. Tian, J. Zhou, and C. Chen, "A review on the application of friction models in wheel-rail adhesion calculation," *Urban Rail Transit*, vol. 7, no. 1, pp. 1–11, Mar. 2021, doi: 10.1007/S40864-021-00141-Y/FIGURES/10.

[27] V. Dmitrievskii, V. Prakht, E. Valeev, A. Paramonov, V. Kazakbaev, and A. Anuchin, "Comparative study of induction and wound rotor synchronous motors for the traction drive of a mining dump truck operating in wide constant power speed range," *IEEE Access*, vol. 11, pp. 68395–68409, 2023, doi: 10.1109/ACCESS.2023.3292244.

[28] S. Nategh, H. Zhang, O. Wallmark, A. Boglietti, T. Nassen, and M. Bazant, "Transient thermal modeling and analysis of railway traction motors," *IEEE Trans. Ind. Electron.*, vol. 66, no. 1, pp. 79–89, Jan. 2019, doi: 10.1109/TIE.2018.2821619.

[29] *EPS Weighting Factors Version 2020d IVL.se*. Accessed: Jan. 3, 2024. [Online]. Available: https://www.ivl.se/english/ivl/publications/publications/eps-weighting-factors—version-2020d.html

[30] J. Wu, *Advances in K-Means Clustering*. Berlin, Germany: Springer, 2012. [Online]. Available: https://link.springer.com/book/10.1007/978-3-642-29807-3, doi: 10.1007/978-3-642-29807-3.

[31] F. Mahmouditabar, A. Vahedi, and N. Takorabet, "Design and analysis of interior permanent magnet motor for electric vehicle application considering irreversible demagnetization," *IEEE Trans. Ind. Appl.*, vol. 58, no. 1, pp. 284–293, Jan. 2022, doi: 10.1109/TIA.2021.3126695.

[32] F. Mahmouditabar, A. Vahedi, M. R. Mosavi, and M. H. B. Bafghi, "Sensitivity analysis and multiobjective design optimization of flux switching permanent magnet motor using MLP-ANN modeling and NSGA-II algorithm," *Int. Trans. Electr. Energy Syst.*, vol. 30, no. 9, Sep. 2020, Art. no. e12511, doi: 10.1002/2050-7038.12511.

[33] A. M. Ajamloo, A. Ghaheri, and E. Afjei, "Multi-objective optimization of an outer rotor BLDC motor based on Taguchi method for propulsion applications," in *Proc. 10th Int. Power Electron., Drive Syst. Technol. Conf. (PEDSTC)*, Feb. 2019, pp. 34–39, doi: 10.1109/PEDSTC.2019.8697586.

[34] S. Gharehseyed, A. Vahedi, A. Nobahari, and A. Darjazini, "Torque characteristics enhancement of ring winding axial flux permanent magnet generator for direct-drive wind turbine," *IET Electr. Power Appl.*, vol. 14, no. 9, pp. 1584–1591, Sep. 2020, doi: 10.1049/iet-epa.2020.0150.

[35] F. Mahmouditabar and N. Baker, "A review on the effect of electrical steel manufacturing processes on the performance of electric machines," *Energies*, vol. 16, no. 24, p. 7954, Dec. 2023, doi: 10.3390/en16247954.

[36] A. Fatemi, N. A. O. Demerdash, T. W. Nehl, and D. M. Ionel, "Large-scale design optimization of PM machines over a target operating cycle," *IEEE Trans. Ind. Appl.*, vol. 52, no. 5, pp. 3772–3782, Sep. 2016, doi: 10.1109/TIA.2016.2563383.

[37] J. Asanuma, S. Doi, and H. Igarashi, "Transfer learning through deep learning: Application to topology optimization of electric motor," *IEEE Trans. Magn.*, vol. 56, no. 3, pp. 1–4, Mar. 2020, doi: 10.1109/TMAG.2019.2956849.

FARSHID MAHMOUDITABAR received the B.Sc. degree from Shahrekord University, Shahrekord, Iran, in 2016, and the M.Sc. and Ph.D. degrees from Iran University of Science and Technology, Tehran, Iran, in 2018 and 2021, respectively, all in electrical engineering. From 2019 to 2021, he was an Electrical Machine and Powertrain Engineer with IKCO, where he designed and manufactured several water-cooled IM for EV applications. From 2021 to 2023, he was also an Electrical Machine and Powertrain Engineer with MAPNA Locomotive Company, where he designed and developed the electrical machines for diesel-electric and over-head powered electric locomotives. In 2023, he joined Newcastle University, as a Research Associate, working on design of electrical machines for manufacture. His main research interests include the design, modeling, and optimization of electrical machines.

NICK J. BAKER (Member, IEEE) received the M.Eng. degree in mechanical engineering from Birmingham University, Birmingham, U.K., in 1999, and the Ph.D. degree in electrical machine design for marine renewable energy devices from Durham University, Durham, U.K., in 2003. He was a Researcher of machine design with Durham University. He was with the Lancaster University's Renewable Energy Group, from 2005 to 2008. He has spent a period in industry as a Senior Consultant of energy consultancy TNEI Services Ltd., Newcastle, U.K., from 2008 to 2010. He is currently with the Newcastle University's Electrical Power Group. He is also a reader in emerging electric machines working on machines across the renewable, automotive, and aerospace sectors.

• • •